

# Automated detection and classification of lunar craters using multiple approaches

Y. Sawabe <sup>a,\*</sup>, T. Matsunaga <sup>b</sup>, S. Rokugawa <sup>a</sup>

<sup>a</sup> Department of Geosystem Engineering, The University of Tokyo, 7-3-1 Hongou, Bunkyo-ku, Tokyo 113-8656, Japan

<sup>b</sup> National Institute for Environmental Studies, 16-2 Onogawa, Tsukuba, Ibaraki 305-8506, Japan

Received 14 October 2004; received in revised form 27 July 2005; accepted 2 August 2005

---

## Abstract

Many missions such as Clementine and SELENE (SELenological and Engineering Explorer) take lunar images for examination. A large volume of imagery data has already been archived and much more is on the way. Extracting the necessary information from the already large and ever growing volume of data is the crucial problem that needs to be overcome.

Craters are studied extensively since they provide us with the relative age of the surface unit and more information on the lunar surface geology. Manually extracting craters from lunar images is a difficult task because it requires a great deal of man power as well as specific knowledge and skills of extraction. Several automated craters detection algorithms have been developed but none is yet practical or sufficiently tested to be reliable.

Our previous algorithm (Sawabe, Y., Matsunaga, T., Rokugawa, S. Automatic crater detection algorithm for the lunar surface using multiple approaches. *J. Remote Sens. Soc. Jpn.* 25 (2), 157–168, 2005.) was improved to enhance detection of craters in lunar images and automate crater classification. This algorithm was tested using various images for wide range of applicability. Four approaches were used with the crater detecting algorithm to find (1) “shady and sunny” patterns in images with low sun angle, (2) circular features in edge images, (3) curves and circles in thinned and connected edge lines, and (4) discrete or broken circular edge lines using fuzzy Hough transform. The algorithm was applied to mare and highland images of the moon captured by Clementine and Apollo under different solar angles and spatial resolution. The new algorithm was able to detect 80% more without parameter tuning. In addition, the detected craters were classified by spectral characteristics derived from Clementine UV–Vis multi-spectral images. Finally, the lunar surface GIS was formulated which has the geological and spectral attributes automatically generated by our algorithm. It could be helpful system to analyze and recognize about the geological settings.

© 2005 Published by Elsevier Ltd on behalf of COSPAR.

**Keywords:** Automatic crater detection; Fuzzy Hough transform; Edge; Clementine; Apollo

---

## 1. Introduction

Recently, many planetary explorations missions were flown and many more are planned. The attention to planets and moons is growing all over the world. In near future, data brought by these missions will help us reveal the unimagined information of planetary science. For example, SELENE, a Japanese lunar orbiting spacecraft to be

launched in 2006, is expected to bring large amount of data to us. However, it is difficult to extract necessary information from massive amount of data in efficient manner.

Craters play an important role to estimate the age of the lunar surface or surface unit when sample specimen is not available (Neukum et al., 1975, 2001). Central peaks of craters suggest materials exhumed from beneath. Studying these peaks could lead to solving the surface crust structures (Tompkins and Pieters, 1999). Furthermore, ejecta analysis of craters in mare suggests the mare lava thickness (Budney and Lucey, 1998). In order to obtain these information, target crater had to be manually extracted from

---

\* Corresponding author. Tel.: +81 3 5841 7036.

E-mail addresses: [sawabe@gpl.t.u-tokyo.ac.jp](mailto:sawabe@gpl.t.u-tokyo.ac.jp), [y-sawabe@crl.hitachi.co.jp](mailto:y-sawabe@crl.hitachi.co.jp) (Y. Sawabe).

images for statistical and morphology data in most recent studies. Manually extracting the craters is already challenging task and further analyzing them takes even more effort. This gave a rise to needs for an algorithm for automatic crater detection. An automated algorithm will help scientists by reducing the laborious task of manually identifying craters. Several automatic and semi-automatic crater detection technique were studied (Burl et al., 2001; Honda et al., 2002), but their accuracy was not enough for crater chronology and they had not been fully tested for practical use. Automatic detection of craters is difficult when their rims are unclear, segmented, or overlapping and when the image is noisy.

A new crater detection algorithm using multiple approaches had been developed and it achieved 80% accuracy (Sawabe et al., 2005) comparing to manual crater detection results by multiple interpreters. This algorithm did not depend on cameras, sun illumination, or spatial resolution. It did not require any parameter tuning either. The Lunar Surface GIS (Geographic Information System) had also been established. It visualizes the surface geological settings and the subsurface structure by utilizing topological and spectral information, including automatic crater detection algorithm, in particular using data from SELENE. When applying this system to SELENE, in particular are focused Multi-band Imager (MI) and Spectral Profiler (SP). MI is a multi spectral and SP is a hyper spectral sensor. This system will help the studies of the crustal structure and the thermal history of the moon using MI and SP data.

In this study, the automatic crater extraction and geographic information system has been improved, that uses the topographic and the spectral information from lunar photos and multi-spectral images. The previous algorithm was greatly improved by including a pyramid representation of an image, this resulted in reduced processing time and higher accuracy. The algorithm was applied to both mare and highland images obtained by Clementine and Apollo images acquired for both mare and highland under different solar elevation. The result were compared with the crater counting results (Neukum et al., 1975) obtained using crater frequency distribution. Craters in the Clementine images were classified with spectral information derived from Clementine UV–Vis multi-spectral images. Finally, a Lunar Surface GIS that showed the surface geological characteristics and the subsurface structure is developed. The topological and spectral information obtained from SELENE data using our automatic crater detection algorithm were mapped in the GIS.

## 2. Data

It is known that the images taken under low sun elevation, such as those from Lunar Orbiter and Apollo are suitable for crater detection (Hiesinger et al., 2003). However, spectral information from multispectral images acquired under high solar elevation is also essential for crater GIS. We used Clementine and Apollo data taken under different

solar elevation to validate our algorithm then Clementine multi-spectral data were used to create the crater GIS.

### 2.1. Apollo data

Apollo photos were taken by metric cameras while orbiting around the moon. These photos were scanned to about 60 m/pixel. To estimate the reliability of our crater detection algorithm, automatic detection results were compared to Neukum et al. (1975) crater counting results. The same areas from same photos that Neukum et al. used were extracted. The areas were the almost homogeneous to obtain primary unmodified crater populations at mare Crisium, Mendeleev, Appennines and Apollo16 landing site. Locations and photo numbers were shown in Table 1. These photos were observed under the low sun elevation.

### 2.2. Clementine UV–Vis data

The lunar Digital Image Model (DIM) produced from Clementine UV/Vis data by US Geological Survey (Isbell et al., 1999) was used in this study. DIM imagery consists of five spectral bands which are radiometrically and photometrically corrected. The images were geometrically controlled at a spatial resolution of 100 m/pixel in sinusoidal equal-area projection, and were observed under the high sun elevation.

These images served as the basis for the production of a number of other data products, including FeO and TiO<sub>2</sub> maps by the method of Lucey et al. (2000) and mineralogical indication by the algorithm of Tompkins and Pieters (1999). Lucey's method for mapping FeO content relies on 750 nm to 950/70 nm reflectance ratio to quantify the spectral effects of ferrous iron in major lunar minerals such as pyroxene and olivine. The technique reduces the comparing effects of the sub-micrometeorite metallic iron that is produced as rocks are exposed to micrometeorite bombardment and solar wind implantation at the lunar surface. In order to estimate TiO<sub>2</sub> content of the surface, Lucey's method utilizes 750 nm to 415/750 nm reflectance ratio. This method is based on the understanding that the Ti-rich opaque mineral ilmenite (FeTiO<sub>3</sub>) has a special effect as a component of a mineral mixture comprising the lunar regolith. Tompkins and Pieters (1999) proposed the mineralogical index using Clementine UV–Vis data. It utilizes a “key ratio” and “spectral curvature”, which are 900/750, 950/750, and 1000/750 nm reflectance ratios and a curve

Table 1  
Apollo photo number and Clementine data number

	Apollo	Clementine	Area (km <sup>2</sup> )
Mare Crisium	AS17-423, 424, 426, 427, 428	17n063	44,109
Appennines	AS17-1819, 1820, 1822, 1825, 1826, AS15-412, 413	24n003	37,198
Apollo16 landing site	AS16-440	10s015	3755
Mendeleev	AS16-344, 347	03n141	32,580

made by 750, 900, and 950 nm reflectance together they are able to, respectively. These parameters are linked to absorption band, the shape of distinguish between low- and high-Ca pyroxene and olivine. They defined 11 mineral classes.

### 3. Methods

#### 3.1. Automatic crater detection algorithm

It is known that the crater feature changes according to its size. Small craters form simple circle, and the larger its size gets the more complex its shape becomes (Heiken et al., 1991). This change in feature posed difficult problem to detect craters with different sizes by a single approach. In our previous algorithm (Sawabe et al., 2005), four different approaches targeting different crater sizes and features were used for crater detection. This algorithm is applicable to images without parameter tuning regardless of their difference in sun elevation, cameras used, and spatial resolutions. This algorithm was further improved in this study by including a pyramid representation of the scale changes of images. It was inserted at the first step of the algorithm flow as preprocessing in Fig. 1. Three different resolution images were processed starting with the lowest resolution. This aimed to improve crater detection accuracy by removing distorted narrow outlines of craters at low-resolution image and to shorten the processing time.

The flowchart of our improved algorithm was shown in Fig. 1. As our previous algorithm was described in elsewhere (Sawabe et al., 2005), we will briefly explain it here. In our algorithm, we defined that a crater is a circular topographical feature in images and the minimum detection crater size is two pixels in radius.

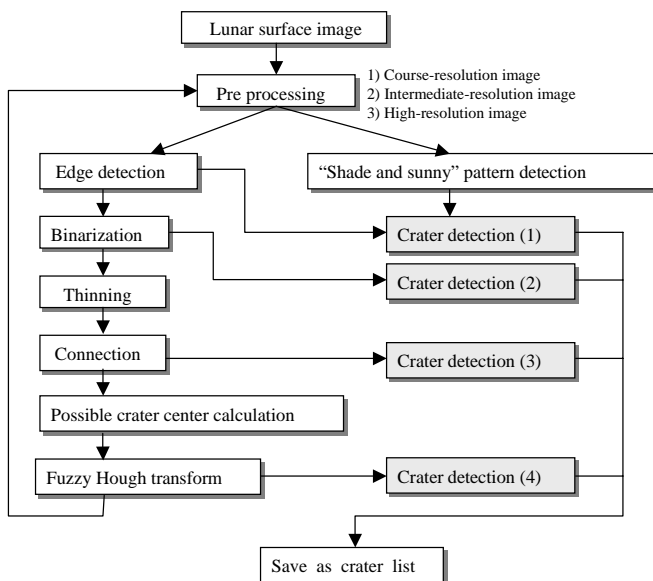


Fig. 1. Flowchart of the proposed automatic crater detection algorithm.

##### 3.1.1. Crater detection (1)

Images were classified into two groups according to sun elevation. If image was taken under low sun elevation, shady and sunny parts of craters are clearly distinguishable. We could recognize this “shade and sunny” pattern in one crater is recognized from the direction of sun radiation. This pattern was detected when the Eq. (1) is satisfied.

$$R_{\min} < R_m - \sigma,$$

$$R_{\max} > R_m + \sigma,$$

(1)

$$p_{\min} < p_{\max},$$

where  $R_{\min}$  indicates the minimum pixel value,  $R_{\max}$  indicates the maximum pixel value and  $\sigma$  indicates the standard deviation in the small area including the target.  $p_{\min}$  and  $p_{\max}$  indicate the position at the minimum and maximum value pixels from the direction of the sun radiation.

A circle was fitted to surrounding edge pixels (Section 3.1.2) of the recognized shady and sunny pattern. The fitted circle was regarded as a crater. If a crater was detected, its edge pixels were deleted from the edge image.

##### 3.1.2. Crater detection (2)

Edge strengths were calculated from images using by the technique based on the height and the reliability of edges (Sugiyama and Abe, 1997). This technique used differences and variances of the nearest pixels and it was appropriate for noisy topographic image such as lunar images. Then edge pixels were detected from edge strength image using the threshold calculated by Kurita et al. (1992)’s technique. If edge pixels form a circular feature, it was recognized as a crater. A circular feature was detected when the roundness  $C$  is more than 0.8.

$$C = 4\pi A/L^2,$$

(2)

where  $A$  is the edge pixels area,  $L$  is the girth of edge pixels.

##### 3.1.3. Crater detection (3)

A set of edge pixels was thinned down to one pixel wide using Hilditch’s thinning algorithm. These lines were connected according to length and direction of the line. If the connected edge lines were closed and the roundness was more than 0.8, the circular form created with these lines is regarded as a crater.

##### 3.1.4. Crater detection (4)

The fourth crater detection method first picks up three points ( $p1 = (x1, y1)$ ,  $p2 = (x2, y2)$ ,  $p3 = (x3, y3)$ ) on one edge line segment selected randomly, and then calculates the center ( $O$ ) of the circle using these points (Fig. 2(a)). This calculation reduces the processing load in next fuzzy Hough transform by narrowing possible crater center existing area. Next, craters were detected using fuzzy Hough transform (Han et al., 1994) that was customized for the sequential detection of circular features. The membership function  $f(p)$  was estimated considering the size-dependent crater distortion.

$$f(p) = e^{-D^2(d,p)/r} \cos \theta,$$

(3)

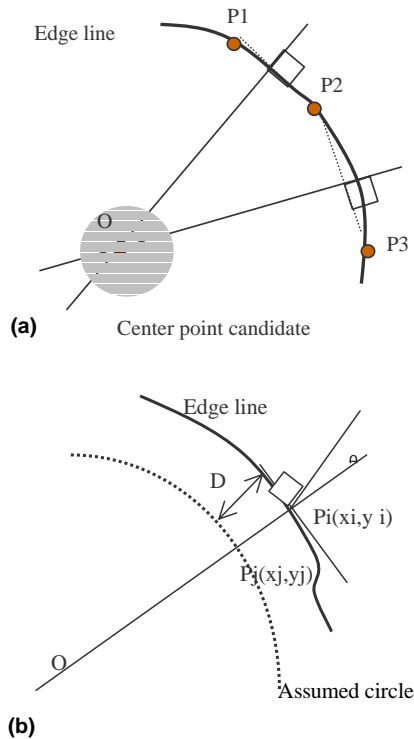


Fig. 2. (a) The voting around the center O of the circle passing through P1, P2, and P3. (b) The relation of edge pixel Pi and the fitted circle (center: O, radius R).

where  $D$ ,  $p$ ,  $r$ ,  $\theta$  are shown diagrammatically in Fig. 2(b).  $D$  is the Euclidian distance from edge line to fitted circle,  $r$  is the radius of the fitted circle, and  $\theta$  is the angle between the normal of the edge line and the radial of the fitted circle.

This step targeted large craters.

### 3.2. Validation method for automatic crater detection algorithm

The advantage of our crater detection algorithm had been described already in Sawabe et al. (2005). The accuracy of our algorithm was more than 80% compared to the manual detection result. In this study, our algorithm was validated by comparing Neukum et al. (1975) crater counts with ours via the crater chronology.

It was shown by Neukum et al. (1975) and Neukum and Ivanov (1994) that cumulative crater distributions measured on geological units of various age could be aligned along a contiguous complex curve with vertical shifts. Approximation of the normalized logarithmic cumulative frequencies with an 11th degree polynomial in  $\log D$  fits the complex structure of the distribution with sufficient accuracy (Neukum et al., 2001; Ivanov et al., 2002). The polynomial has the form:

$$\log N = a_0 + \sum_{n=1}^{11} a_n (\log D)^n, \quad (1)$$

where  $D$  is a diameter of the crater in km and  $N$  is the number of craters per  $\text{km}^2$ .  $a_0$  represents the intercept at 1 km

in diameter. Eq. (1)'s coefficients are as follows:  $a_1 = -3.557528$ ,  $a_2 = 0.781027$ ,  $a_3 = 1.021521$ ,  $a_4 = -0.156012$ ,  $a_5 = -0.444058$ ,  $a_6 = 0.019977$ ,  $a_7 = 0.086850$ ,  $a_8 = -0.005874$ ,  $a_9 = -0.006809$ ,  $a_{10} = 0.000825$ ,  $a_{11} = 0.0000554$ .

The empirically derived chronology by Neukum and Ivanov (1994) is given by

$$N_{\text{cum}}(D \geq 1 \text{ km}) = 5.44 \times 10^{-14} \{\exp(6.93t) - 1\} + 8.38 \times 10^{-4} t, \quad (2)$$

where  $t$  is time in billion years.

The statistical error  $\sigma$  is explained as follows:

$$\sigma = (n \pm \sqrt{n})/A, \quad (3)$$

where  $n$  is the number of  $n$ th craters and  $A$  is the surface area.

In this study, Eqs. (1) and (2) were used to fit the crater detection results by the least-square method and calculate surface absolute ages.

### 3.3. Visualization system

Our visualization system, Lunar Surface GIS, utilizes Clementine images, reflectance, FeO wt% and  $\text{TiO}_2$  wt% which were calculated using Lucey's method (Lucey et al., 2000). On all images, outlines of detected craters are drawn. Tompkins' mineralogy derived from average spectral information of the interior of detected craters. In the reflectance image, craters are distinguished by different colors according to their attributes. These images can be shown in two or three-dimensional space. Latitude and longitude are depicted at four corners of image and the diameter labels are added to major craters.

## 4. Results

In this chapter, results of our algorithm analyzing Clementine UV-Vis and Apollo data at four sites are shown. This improved algorithm could reduce the processing time by about one-fourth. Additionally, detected craters were visualized using the proposed crater GIS to make understanding of the geological setting much easier.

Note there are some factors of the estimated age error by crater counting as follows: (1) error in the equation about the relation between the crater number and the surface age. (2) error about the statistics of crater number. (3) error of crater counting. We did not consider error (1) in this paper. Error (2) was indicated as  $\pm\sigma$  (Eq. (3)) with estimated age. The difference between our estimated age and Neukum's age shows error (3).

### 4.1. Crater detection results

#### 4.1.1. Mendeleev ( $5.7^\circ\text{N}/140.9^\circ\text{E}$ 313 km in diameter)

The interior of this large crater seemed to be flat. Neukum et al. (1975) had truncated craters smaller than 3 km in diameter to avoid unrecognized secondary craters. How-



ever, all craters larger than 4 pixels (about 240 m) in diameter were detected by our algorithm. Automatically detected results of a part of Mendelev were shown in Fig. 3. It is shown that craters were detected well both in Apollo and Clementine images. A few craters which were not detected only appeared in Apollo image. This was caused by failing to recognize edge pixels at the binarization step in Clementine image. These undetected craters were recognized these even by human-eyes in Clementine image, detecting craters from high sun elevation and low

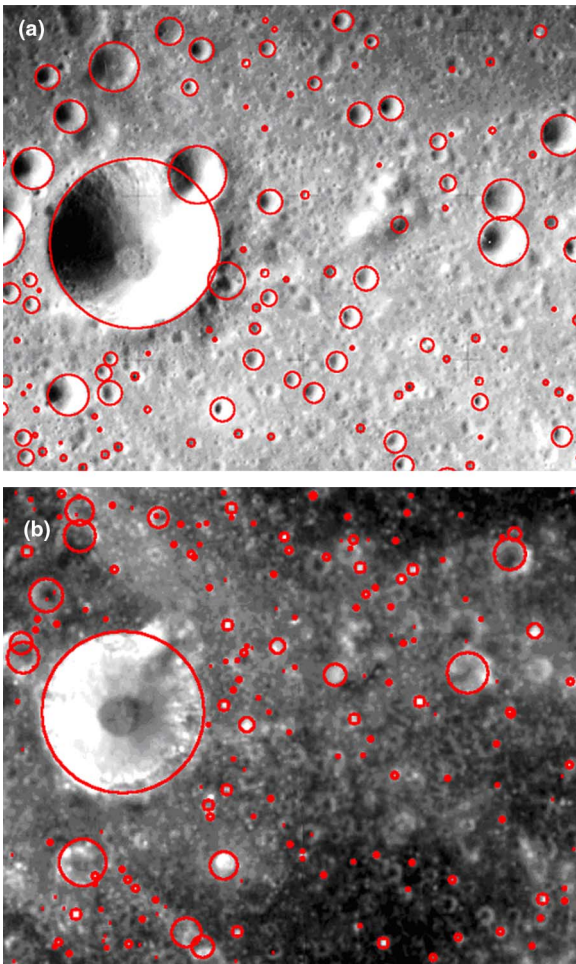


Fig. 3. Crater detection results using the proposed automatic algorithm at a part of Mendelev. (a) Apollo image (830 × 673 pixels), whole image detection rate is 81%, manual detection number: 281, automatic detection number: 285, (b) Clementine image (600 × 500 pixels), whole image detection rate is 85%, manual detection number: 86, automatic detection number: 110.

Table 2  
Calculated surface ages

	Neukum	Automatic Apollo	Automatic Clementine
Mare Crisium	$3.0 \pm 0.2$	$3.0 \pm 0.2$	$3.2 \pm 0.2$
Apennines	$3.8 \pm 0.0$	$3.8 \pm 0.0$	$3.9 \pm 0.1$
Apollo16 landing site	$3.9 \pm 0.0$	$3.9 \pm 0.0$	$3.9 \pm 0.0$
Mendelev	$4.0 \pm 0.0$	$3.9 \pm 0.0$	$4.0 \pm 0.0$

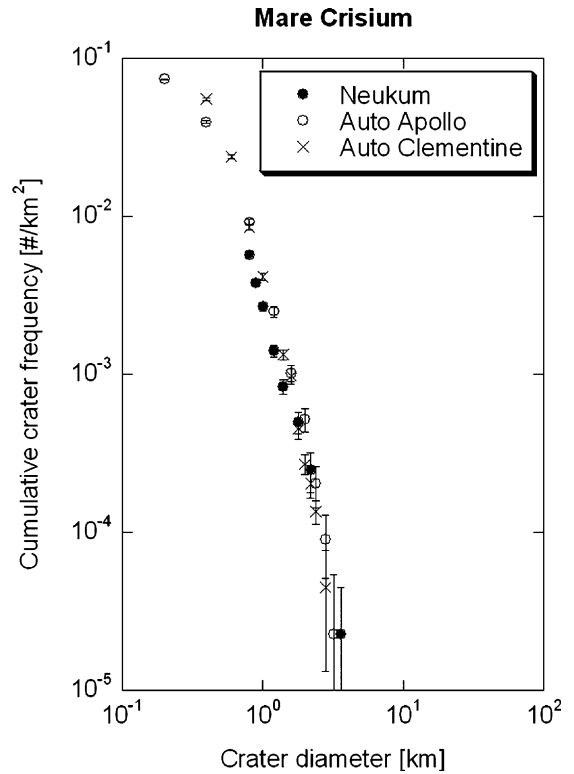


Fig. 4. Cumulative size-frequency distribution of automatic detection results of Apollo and Clementine image, and the results of Neukum et al. (1975) at the eastern part of Mare Crisium.

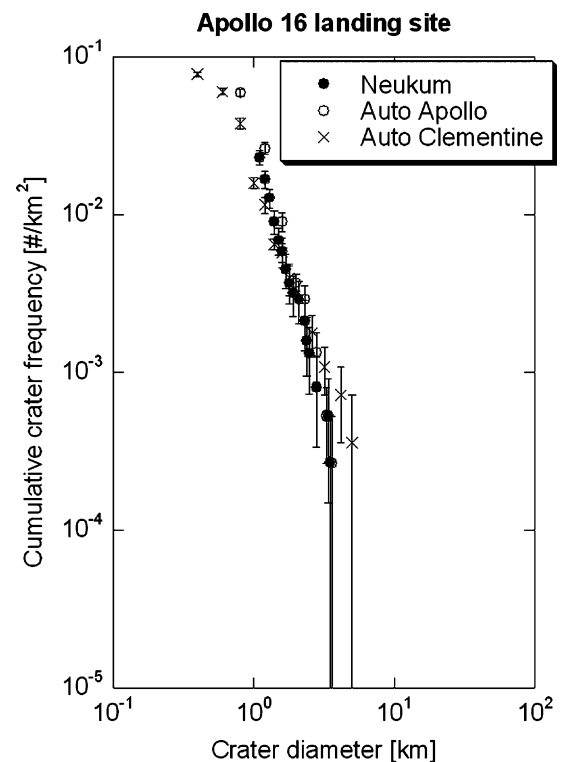


Fig. 5. Cumulative size-frequency distribution of automatic detection results of Apollo and Clementine image, and the results of Neukum et al. (1975) at Apollo 16 landing site.

spatial resolution images still remains as a great task. For further details of the crater detection differences using images taken at various settings, see Sawabe et al. (2005).

As far as numbers of detected craters goes, automatic detection results were almost same as the manual results.

The same area from Clementine and Apollo data used by Neukum et al. (1975) was used. As Neukum described only counting numbers of craters we calculated surface age by Eqs. (1) and (2) using that counting result and automatic detection results. The calculated ages were presented in Table 2. The age by Apollo automatic detection was 0.1 b. y. younger than others.

#### 4.1.2. Mare Crisium (13.4°N–18.3°N/56.0°E–65.4°E)

Neukum et al. (1975) selected the eastern part of mare Crisium because the whole mare is not homogeneous. The counting results by manual and automatic methods shown in Fig. 4 on a log–log plot and calculated ages were presented in Table 2. Fig. 4 indicates good agreement

between Neukum counting and automatic detection results. However, automatic detection results of those smaller than 1.4 km in diameter from both Apollo and Clementine showed slightly better than Neukum's. Automatic detection for Clementine and Apollo gave almost same results for craters larger than 0.8 km in diameter despite their differences in spatial resolution and sun illumination. Calculated ages in Table 2 indicates consistent results within the error bars. However, Clementine result is 0.2 b. y. older than others. It is because there were few undetected craters larger than 3.0 km in diameter.

#### 4.1.3. Apollo 16 landing site (9°S/15.5°E) and Apennines (18.9°N/3.7°W)

Apollo 16 landing site looks very flat and homogeneous. Manual and automatic detection results were shown in Fig. 5. They were plotted on the same line. At larger sizes, the automatic result from Clementine was slightly more frequent than others, because estimated sizes of craters

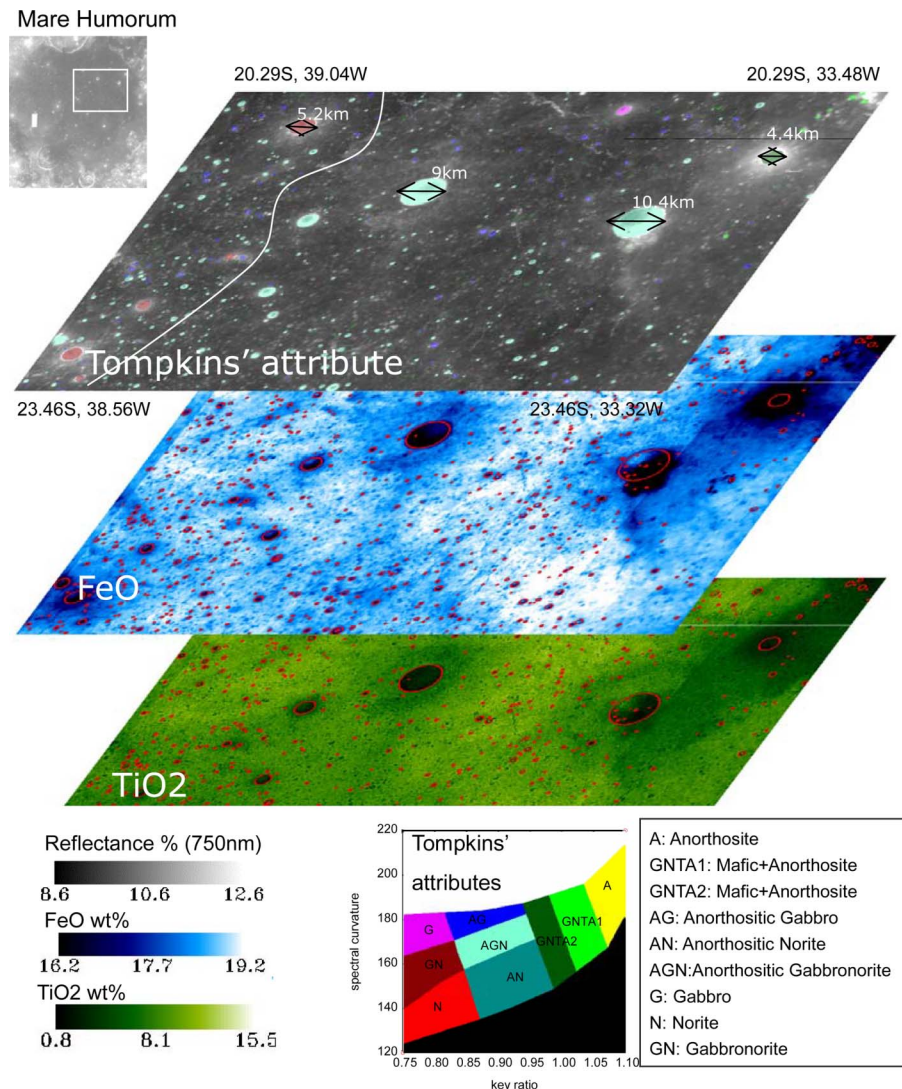


Fig. 6. Reflectance at 750 nm, FeO contents and TiO<sub>2</sub> contents image with crater outlines as three dimensions. At reflectance image, craters were colored based on Tompkins' mineralogy using average reflectance of crater interior.

were larger than Apollo. Neukum had eliminated some craters as probable secondary ones. Therefore, their result was less frequent than automatic results at smaller size. All three crater detection results demonstrated the same surface age (Table 2). Apennines results also indicated good agreement between manual and automatic results.

#### 4.2. Visualization

By adding lithological and chemical attributes to detected craters, geological settings of lunar craters are more clearly displayed. For example Clementine data were applied to visualize surface geology of Mare Humorum (Fig. 6).

Dark areas have less FeO and TiO<sub>2</sub> contents than the brighter surroundings. By drawing outlines of craters, the reason of the difference of FeO and TiO<sub>2</sub> contents could be recognized in local view. The surroundings of the upper right crater seem to have less FeO and TiO<sub>2</sub>. It is likely that this crater had excavated the highland material beneath the mare lava. Furthermore four craters at left and five craters at the center of the image have different Tompkins' mineralogy index colors in spite of their similarity in size and location. It is probably because there is the boundary of the geological units between differently colored craters. An example of the boundary is shown in Fig. 6.

It is useful to interpret the geological setting through this Lunar Surface GIS.

#### 5. Conclusions

In this study the automatic crater detection and classification algorithm described in Sawabe et al. (2005) was further improved. It can be applied to different kinds of images without parameter tuning regardless of the difference in cameras used, sun elevation and spatial resolution. This automatic algorithm could detect craters of all sized and shapes with 80% accuracy. Addition of preprocessing step, the changed spatial resolution as a pyramid resulted in shorter the processing time by one-fourth.

The improved algorithm was applied to Apollo and Clementine images for validation. The result was compared to the manual crater detection result obtained by Neukum et al. (1975) using crater frequency distribution. The derived crater frequency tendencies shows good agreement and ages calculated were almost same. Craters detected by our algorithms can be used in lunar chronology studies.

The lunar surface GIS uses spectral information and crater detection results. By adding lithological and chemical attribution from spectral data, geological settings of lunar craters are displayed more clearly.

In the future, our Lunar Surface GIS is expected to automatically acquire more geological information such as the surface age, the ejecta distribution and the mare lava thickness.

#### Acknowledgements

We thank the National Space Science Data Center through the World Data Center for Satellite Information, groups of 71-063A-03B, 72-031A-03A, and 72-096A-07A, for providing Apollo photographs. The present research was supported (in part) through the 21th Century COE Program, "Mechanical System Innovation", by the Ministry of Education, Culture, Sports, Science and Technology.

#### References

- Budney, C.J., Lucey, P.G. Basalt thickness in mare Humorum: the crater excavation method. *J. Geophys. Res.* 103 (E7), 16855–16870, 1998.
- Burl, M.C., Stough, T., Colwell, W., Bierhaus, E.B., Merline, W.J., Chapman, C., Automated detection of craters and other geological features, in: *Proc. i-SATRAS-01*, AM118, 2001.
- Han, J.H., Koczy, L.T., Poston, T. Fuzzy Hough transform. *Patt. Recogn. Lett.* 15, 649–658, 1994.
- Heiken, G.H., Vaniman, D.T., French, B.M. *Lunar Source Book*. The University of Cambridge, 1991.
- Hiesinger, H., Head, W.H., Wolf, U., Jaumann, R., Neukum, G. Ages and stratigraphy of mare basalts in Oceanus Procellarum, Mare Nubium, Mare Cognitum, and Mare Insularum. *J. Geophys. Res.* 108 (E7), doi:10.1029/2002JE001985, 2003.
- Honda, R., Iijima, Y., Konishi, O. Mining of topographic feature from heterogeneous imagery: its application to lunar craters. *Progress of Discovery Science*, LNAI pp. 395–407, 2002.
- Isbell, C.E., Eliason, E.M., Adams, K.C., Becker T.L., Bennett, A.L., Lee, E.M., McEwen, A., Robinson, M., Shinaman, J., Weller L.A., Clementine: a multi spectral digital image model archive on the moon (abstract #1822), 30th Lunar and Planetary Science Conference CD-ROM.
- Ivanov, B.A., Neukum, G., Bottke Jr., W.F., Hartmann, W.K. The Comparison of Size-Distributions of Impact Craters and Asteroids and the Planetary cratering rate, *Asteroids III*. University of Arizona, 2002, pp. 89–101.
- Kurita, T., Otsu, N., Abdelmalek, N. Maximum likelihood thresholding based on population mixture models. *Pattern Recogn.* 25 (10), 1231–1240, 1992.
- Lucey, P., Blewett, D.T., Jolliff, B.L. Lunar iron and titanium abundance algorithms based on final processing of Clementine ultraviolet–visible images. *J. Geophys. Res.* 105 (E8), 20297–20305, 2000.
- Neukum, G., Konig, B., Arkani-Hamed, J. A study of lunar impact crater size-distributions. *The Moon* 12, 201–229, 1975.
- Neukum, G., Ivanov, B.A., Crater size distributions and impact probabilities on earth from lunar terrestrial-planet, and asteroid cratering data, *Hazards due to comets and asteroids*, University of Arizona, p. 359, 1994.
- Neukum, G., Ivanov, B., Hartmann, W.K. *Cratering Records in the Inner Solar System, Chronology and Evolution of Mars*, vol. 55–86. Kluwer, Dordrecht, 2001.
- Sawabe, Y., Matsunaga, T., Rokugawa, S. Automatic crater detection algorithm for the lunar surface using multiple approaches. *J. Remote Sens. Soc. Jpn.* 25 (2), 157–168, 2005.
- Sugiyama, T., Abe, K., 1997. Edge feature analysis by a vectorized feature extractor and in multiple edge. *IEIC, D-2, J80-D-2*, 6, pp. 1379–1389, 1997 (in Japanese).
- Tompkins, S., Pieters, C.M. Mineralogy of the lunar crust: Results from Clementine. *Meteorit. Planet. Sci.* 34, 25–41, 1999.